


Dendritic deformation modes in additive manufacturing revealed by operando x-ray diffraction

Adrita Dass ¹, Chenxi Tian¹, Darren C. Pagan^{2,3} & Atieh Moridi ¹✉

Dynamic solidification behavior during metal additive manufacturing directly influences the as-built microstructure, defects, and mechanical properties of printed parts. How the formation of these features is driven by temperature variation (e.g., thermal gradient magnitude and solidification front velocity) has been studied extensively in metal additive manufacturing, with synchrotron x-ray imaging becoming a critical tool to monitor these processes. Here, we extend these efforts to monitoring full thermomechanical deformation during solidification through the use of operando x-ray diffraction during laser melting. With operando diffraction, we analyze thermomechanical deformation modes such as torsion, bending, fragmentation, assimilation, oscillation, and interdendritic growth. Understanding such phenomena can aid the optimization of printing strategies to obtain specific microstructural features, including localized misorientations, dislocation substructure, and grain boundary character. The interpretation of operando diffraction results is supported by post-mortem electron backscatter diffraction analyses.

¹Sibley School of Mechanical and Aerospace Engineering, Cornell University, Ithaca, NY 14850, USA. ²Cornell High Energy Synchrotron Source, Cornell University, Ithaca, NY 14850, USA. ³Present address: Department of Materials Science and Engineering, The Pennsylvania State University, University Park, PA 16802, USA. ✉email: moridi@cornell.edu

Metal Additive Manufacturing (AM), specifically laser beam-based AM of alloys, is a non-equilibrium process that builds components layer-by-layer using digital models^{1–6}. Extreme cooling rates and temperature gradients are distinguishing features of these processes compared to standard thermomechanical processing^{7,8}. These extreme thermo-mechanical states produce conditions that generate complex final microstructures⁹. First, the small size of the melt pool during AM leads to limited nucleation events, suppressing the conditions favorable for equiaxed grain formation^{10,11}. Also, solute accumulation ahead of the growth front can cause constitutional undercooling that can give rise to dendritic solidification^{12–14}. Dendritic growth is followed by interdendritic solidification caused by local solute enrichment in the fluid gaps between the remaining dendrites¹⁵. The final as-built microstructure is a culmination of these evolution stages at fast time scales, making it challenging to study them using traditional approaches.

Dendritic growth during solidification has been the subject of numerous in-situ imaging studies, deepening our understanding of such fundamental mechanisms. The dendritic growth mechanisms during solidification were studied for Al-Cu alloys at controlled cooling rates to demonstrate the feasibility of detecting stray dendrites and designing localized microstructures¹⁶. X-ray imaging of the dendritic deformation mechanisms at cooling rates closer to casting has also been studied. Some examples include deformation in nickel-based superalloys such as bending and torsion, ultimately influencing the final dendritic network^{17,18}, mechanisms of dendrite fragmentation, and their influence on columnar to equiaxed transition^{19,20}. In-situ dynamic transmission electron microscopy (DTEM)²¹ is another emerging technology that provides high-quality solidification data with exposure times down to 15 μs , however, they are limited by the overall maximum sample volume of 1500 μm^3 . Proton radiography, on the other hand, could be used for imaging bulk metallic volumes, albeit compromising spatial resolution and being limited by phase contrast of the alloy systems²².

From the above examples, it is evident that even though the imaging techniques give us a wealth of information about the fundamentals of the solidification process, they have several challenges such as: (i) only metallic systems having sufficient phase contrast can be studied (lighter vs. darker phase); (ii) there is no information about lattice orientation and structure or the thermomechanical state of the material, which influences final as-built solidification microstructures²³.

In this paper, we propose the use of operando synchrotron diffraction during AM of Inconel 625 (IN625) superalloy to study the effects of solidification dynamics on various dendrite deformation mechanisms. This approach eliminates some of the constraints pertinent to imaging, enabling quantification of in-situ deformations, the ability to extend to versatile material systems (not limited by phase contrast) and capturing high-speed dynamics with sufficient spatial and temporal resolution relevant to AM. Overall, operando synchrotron diffraction provides direct information on the microstructural and thermomechanical evolution during the AM process, contributing to an in-depth understanding of solidification mechanisms. This approach leads to improved high-fidelity datasets, which inform predictive models for microstructure evolution.

In this study, time-dependent analysis of diffracted x-ray intensity is used to examine the effects of thermomechanical loading on dendrite formation behavior that occur during laser melting of IN625. The experiment was performed at the Cornell High Energy Synchrotron Source-FAST beamline using a custom AM setup²⁴ with x-rays in transmission mode. More information about the experimental setup can be found in the Methods and Supplementary Fig. 1 and an illustration is provided in

Supplementary Fig. 2. Specifically, we study (i) dendrite deformation mechanisms during different solidification stages at fast temporal resolution using azimuthal angle, η versus time relationships directly from raw 2D x-ray datasets; and (ii) the nature of staggered dendritic and interdendritic growths along with the formation of secondary phases. During standard 1D diffraction analyses, discrete values of ' η ' are lost after azimuthal integration, which could otherwise provide information about intergranular misorientations²⁵. Therefore, only the lattice strains can be measured after data reduction, i.e., after azimuthal integration along the diffraction ring. Our approach of directly analyzing raw datasets preserves rich process information by giving specific information on η as well as radial direction information. In addition, by combining the results of the operando diffraction with post-mortem electron backscatter diffraction (EBSD), we are able to identify and quantify specific signatures of dendritic deformation mechanisms and the origins of misorientation and its evolution during AM solidification. The time-resolved data will help us understand the sequence of deformations at various stages of solidification to ultimately form a link between localized growth mechanisms and the final-as-built microstructure. Through this work, we contribute to the growing body of research aimed at advancing the understanding and optimization of solidification processes in AM.

Results and discussion

Identification of dendritic deformation modes and correlation via post-mortem electron backscatter diffraction. First, we present diffracted intensity measured operando in the form of azimuthal angle η around a diffraction ring versus time t to clearly distinguish distinct features related to the dendritic deformation mechanisms in Fig. 1a, b, c and 2a. Out of five peaks captured within our 2θ range, {311} and {222} had the highest intensities and captured interesting deformation mechanisms during various stages of solidification and hence have been used for further analyses. Since a representative number of grains were not probed, the phenomena that we are going to discuss are likely influenced by local grain neighbours and mechanical anisotropy.

In the geometry employed, the diffracted intensity monitored is associated with lattice planes with normal along the build direction. Unlike more common changes in Bragg angle 2θ that provides information about lattice plane spacing and crystal structure, changes in the azimuthal angle of diffracted intensity provide information about the rotations of lattice planes within the probed grains. It is worth mentioning that tracking motions is more difficult during the early stages of solidification as the solid can either move out of Bragg diffraction condition or the window captured by the x-rays. This is typically the case for the motion/rotation of minimally constrained equiaxed dendrites in the melt pool. However, tracking deformations of the already anchored dendrite is easier, and it shows up as smaller changes along the azimuth. Therefore, dendritic deformations during the latter stages of solidification can be continuously tracked in constrained regions. In the figures, intensity fluctuations in time at a fixed angle correspond to sets of lattice planes within grains moving in and out of the diffraction condition due to rotation about an axis transverse to the x-ray beam direction, straight vertical intensity corresponds to stationary sets of lattice planes, intensity smoothly shifting in azimuthal angle with time indicate rotation of lattices planes about an axis parallel to the incoming x-ray beam^{26,27}, and oscillatory motion of intensity in the azimuthal angle corresponds to oscillating of lattice plane orientation about the incoming x-ray beam axis.

As shown in Fig. 1a, the intensity evolution from the {311} family of lattice planes indicates distinct features of the melt pool,

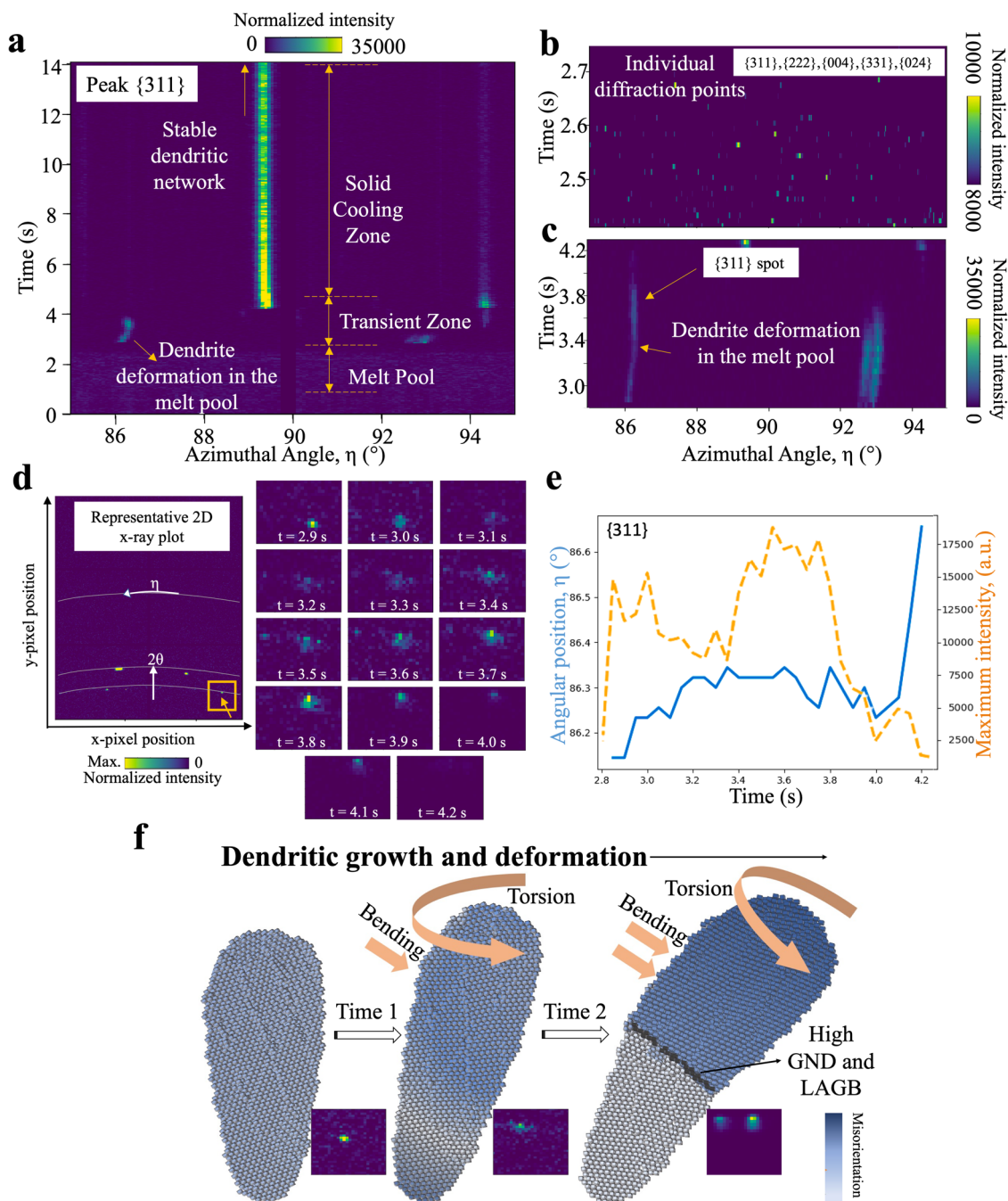


Fig. 1 Deformation modes in growing dendrites during solidification. **a** Azimuthal angle (η) versus time plot for IN625 {311} peak, processed at 250 W laser power, 4.5 mm/s scan speed, showing different stages of solidification; **(b)** Azimuthal angle (η) versus time plot for all five IN625 peaks between 2.4 s to 2.7 s, showing crystallites resulting in individual diffracting points; **(c)** Azimuthal angle (η) versus time plot for IN625 {311} peak between 2.8 s to 4.2 s, highlighting the primary dendritic growth and its deformation; **(d)** representative 2D x-ray diffraction plot at a specific timeframe, with orange box specifying the region of interest. White curved lines along the actual azimuth ring are shown for reference. The individual 2D x-ray diffraction plots of only the region of interest are tracked from $t = 2.9$ s to $t = 4.2$ s, averaging ten frames per timestep for better statistics **(e)** The angular position (η) and the absolute maximum intensity (a.u.) on the detector versus time plot for the same point being tracked in **(d)**; **(f)** The schematic of the deformation modes in the dendrite as a result of torsion and out-of-plane bending. Note that all scale bars are normalized intensities.

transient zone, and the solid cooling zone passing through the x-ray diffraction volume. Initially, the x-ray beam probes the melt pool, as negligible intensity is measured, indicating lack of crystalline solids. This is followed by the transient zone, wherein we observe the intermittent appearance of diffracted intensity and rapid shifts in intensity and azimuthal angle that we associate with various mechanisms of dendritic growth and deformations. Lastly, the solid cooling zone is defined by no or minimal changes

to diffracted intensity. Figure 1b shows a detailed view of the appearance of intensity due to the formation of small crystallites in the early stages of solidification, which move out of diffraction conditions likely due to the strong melt pool convection effects²⁸. These are likely minimally constrained equiaxed dendrites, which move within the melt pool and rapidly transition out of Bragg diffraction condition. After this stage, relatively smaller motions of lattice planes are observed as the fraction of solids in the

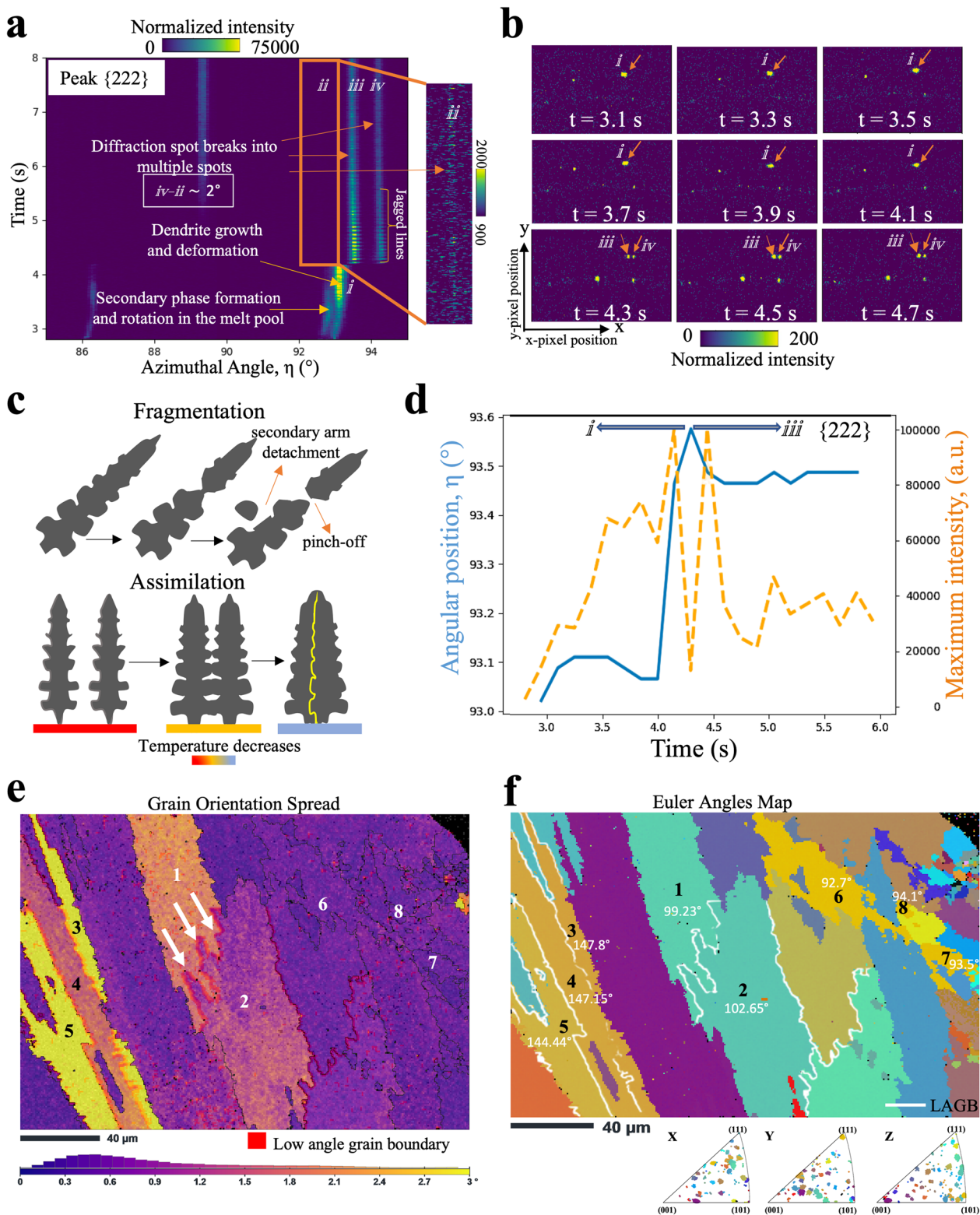


Fig. 2 Secondary phase formation, spot splitting and oscillations in diffraction data and correlations to post-mortem EBSD. **a** Azimuthal angle (η) versus time plot for IN625 {222} peak focused on the solidification and solid cooling zone, processed at 250 W, 4.5 mm/s. The special events are annotated in the figure. Inset shows the appearance of a straight line after adjusting normalized intensity in that area; **(b)** 2D x-ray diffraction plots of one region of interest, with orange arrows focusing on the spot being tracked. The time range is from $t = 3.1$ s to $t = 4.7$ s to focus on the spot-splitting phenomenon; **(c)** The schematic of the pinch-off and secondary arm detachment and dendrite assimilation mechanisms; **(d)** The angular position (η) and the absolute maximum intensity (a.u.) on the detector versus time plot for the same spots being tracked in **(a)** and **(b)**; **(e)** EBSD image of the sample cross-section, highlighting intragranular misorientations and low-angle grain boundaries (LAGB); **(f)** Euler angle map numbering groups of grains which could have undergone possible bending (1, 2), fragmentation (6, 7, 8) or assimilation (3, 4, 5), along with the simulated azimuthal values for each grain. Note that all scale bars are normalized intensities.

transient zone increases. An example is shown in Fig. 1c, wherein the curved line from 2.9 s at $\eta = 86.5^\circ$ corresponds to an azimuthal change of about $\sim 0.5^\circ$. This could be associated with a directional dendrite undergoing deformation in the transient zone due to an interplay of fluid, drag, and gravity forces. Upon closer observation of the time-dependent evolution of the same diffraction peak in Fig. 1d (also in Fig. 1a, c between $t = 2.9$ to 4.2 s), we see an appreciable spread along the azimuthal $\{311\}$ curve with fluctuations in intensity from a bright to a misty-dull-like pattern, followed by a more brilliant spot again, ending with a misty-dull pattern. Figure 1e quantifies the time-resolved shift in azimuthal angular position and fluctuations in the peak's absolute maximum intensity (a.u.). The spread along azimuth is due to a distribution of lattice plane orientation developing in the dendrite due to thermomechanical deformation, while the intensity fluctuations can be associated with rigid rotation of the entire dendrite due to either bending or torsion depending on the dendrite's orientations, along the build direction or transverse respectively. This is schematically shown in Fig. 1f. In the first image, the crystallite domain remains undistorted, resulting in crystallites that are oriented in the same direction, causing a sharp spot on the x-ray detector without any spreading. However, at time 1, the crystalline domain undergoes torsion and bending, leading to changes in misorientation that result in a spread along the azimuth. Further, it is possible to quantify the misorientation development, namely torsion and bending modes based on diagonal and off-diagonal terms in the curvature tensor from the EBSD analysis. The curvature tensor is defined as the directional derivative of disorientations between neighboring points. Specifically, Supplementary Fig. 3c shows the six components of the curvature tensor, with the diagonal elements (K_{11} , K_{22}) signifying contributions due to torsion and off-diagonal elements (K_{12} , K_{21} , K_{31} , K_{32}) to bending, respectively^{29,30}. Therefore, post-mortem EBSD analysis helps us quantify the observed changes in x-ray diffraction patterns, including the spread along azimuth and intensity fluctuations due to thermomechanical deformation in the dendrite.

Examining the evolution of diffracted intensity in the azimuthal angle versus time for the $\{222\}$ sets of lattice planes (shown in Fig. 2a, b) provides an opportunity to observe other mechanisms during solidification. Three events are observed here including: (i) the appearance of a crystallite which we propose corresponds to the formation of a secondary phase rotating in the melt pool, and (ii) a prominent dendrite beside the secondary phase, as highlighted during $t = 3.1$ s to 4.7 s, suddenly splits into at least two spots, and (iii) the resultant dendrites from (ii) appear as jagged lines which could be due to the oscillatory motion of the diffracting domains, causing it to move in-and-out of the diffraction condition periodically. According to energy dispersive spectroscopy (EDS) analysis presented in Supplementary Fig. 4b and Supplementary Table 1a, the secondary phase crystallite in the first observation is identified as an Nb_2C carbide particle. Possible mechanisms for the second observation are schematically shown in Fig. 2c and include fragmentation of dendritic trunks or the secondary arms from the parent dendrite due to shape instabilities based on local dendritic geometries²⁰ or assimilation of the dendritic trunks due to contraction of the substrate during cooling, leading to consuming the secondary arms and forming a low angle grain boundary (LAGB)¹⁸. These possible mechanisms coincide with an abrupt shift of intensity in the azimuthal direction and strong intensity fluctuations, as quantified in Fig. 2d. For the jagged lines in (iii), the oscillatory movement is first observed at the frequency of approximately ~ 50 Hz, which decayed to ~ 17 Hz after further cooling (Supplementary Fig. 5). The frequency of the oscillations (>15 Hz) rules out damp-down vibrations of the stepper motor (13 Hz) and fluctuations of the

incoming x-ray beam (<0.1 Hz). Moreover, the material is completely solidified when oscillations commence, as evidenced by our calculations of cooling rates extracted from the lattice spacing vs. time curves (as shown in Supplementary Fig. 6). This eliminates the possibility of fluid flow caused by the Marangoni effect as the reason behind the observed oscillations. We propose that the observed oscillatory behavior is likely due to thermally induced vibrations occurring after the laser is switched off (at 4.1 s)³¹. While there is a possibility that the oscillations occur due to radial motions of diffraction peaks in the material, the high energy of the x-rays (along with a relatively flat Ewald sphere) results in broad diffraction peaks. Thus, the likelihood of the exits from the diffraction condition is higher due to azimuthal motions of the peak (lattice rotation) as opposed to radial motions (lattice strain). In this case, for the peaks to enter and exit the diffraction conditions, the strain fluctuations need to exceed the energy bandwidth of the incoming x-ray beam (i.e., $1e^{-3}$).

To confirm the deformation phenomena observed during operando diffraction experiments, we performed post-mortem EBSD analysis on the same sample to measure the final spatial orientation fields. If sufficiently large, the thermomechanical deformations that are a combination of torsion and bending phenomena can lead to the emergence of permanent plastic deformation which will generally be accommodated by geometrically necessary dislocations (GND). The GNDs generate permanent lattice misorientation which can be measured with EBSD and, in addition, these GNDs can self-organize to form LAGBs. This phenomenon has been demonstrated in Fig. 1f, wherein at time 2, further bending and torsion results in significant differences in misorientations across different parts of the domain, leading to two distinct spots on the x-ray detector. These findings are consistent with previous studies that have shown higher misorientation accumulation towards the last part of the grain that solidifies²³. Therefore, the azimuthal spread is a direct function of the misorientation development in the diffracted spot. As quantified from EBSD in Fig. 2e, the median intragranular misorientation distributions within grains likely caused due to the torsional forces is estimated to be $0.45\text{--}0.52^\circ$. This value is in close agreement with 0.5° change along the azimuth in Fig. 1e. Also, we observe regions with higher degrees of misorientation on this map (Fig. 2e), which corresponds to high GND densities (Supplementary Fig. 3b) with LAGB formation at the interface between grains. Two-grain groups, namely 1–2 and 3–5 exhibit these phenomena, which is likely formed to accommodate the bending-induced lattice curvature (the white arrows in Fig. 2e), or which could be a possible grain assimilation phenomenon (as shown schematically in Fig. 2c) to accommodate differences in their orientation when two dendrites join laterally due to contractions. Quantitative analysis of the final curvature of the lattice is provided in Supplementary Fig. 3c.

A detailed procedure was developed to correlate the EBSD data to x-ray diffraction data (refer to Methods and Supplementary Fig. 7). This procedure involves mapping any particular grain from the EBSD Euler angle map to its appearance on the 2D x-ray detector. The EBSD Euler angle map contains spatial orientation information for every individual crystal, which helps obtain the crystal orientation relative to the EBSD detector orientation, and its corresponding diffraction spot on the x-ray detector. We note that uncertainties may arise with this approach since only a 2D cross-section of the sample is examined with EBSD as opposed to a 3D volume with the x-rays; nevertheless, we were able to identify feasible candidates for the spot splitting phenomena during operando diffraction experiments following this approach. Grains 1–2 are likely formed to accommodate the bending-induced lattice curvature (the white arrows in Fig. 2e), causing a maximum misorientation of $\sim 3.5^\circ$ from simulated x-ray data. The

grain group 3–5 undergoing possible dendritic assimilation in Fig. 2f would have appeared with azimuthal angle values of 147.8°, 147.15°, and 144.44° (with maximum changes of ~2.7°) on the x-ray detector. This matches well with our observations on the x-ray azimuthal plot in Fig. 2a, with the values lying between $i = 92.86\text{--}93.32^\circ$ (before spot splitting) and $ii = 92.43\text{--}92.62^\circ$, $iii = 93.40\text{--}93.68^\circ$, and $iv = 94.10\text{--}94.30^\circ$ (after spot splitting), respectively. Similarly, another possible candidate undergoing fragmentation for the observed spot splitting in the detector could be the grain group 6–8, with the corresponding azimuthal angle projection values for these grains as 92.6996°, 93.5299°, and 94.1063°, respectively (with maximum changes ~1.5°). Since these grains have orientations (Euler angles) very similar to each other, it is evident that they either assimilated to form a larger grain (grain group 3–5) with an accumulation of LAGB or fragmented from the initial parent grain (grain group 6–8).

Evidence of interdendritic growth and formation of secondary phases. To this point, we have analyzed the evolution of diffracted intensity azimuthally to understand the rotation of the lattice during the thermomechanical loading during solidification. Next, we will analyze the evolution of intensity along the Bragg angle 2θ with time, which as mentioned, provides information regarding lattice plane spacing and structure. The azimuthally integrated intensity versus time is shown in Fig. 3. The peak shoulders appear during 3.7 s to 4.9 s due to the non-homogeneous cooling of the sample processed under the laser, causing appreciable shifts in 2θ for intensity associated with {222} lattice planes. This is inevitable due to the 1 mm print thickness along the x-ray transmission direction, resulting in temperature variation across thickness. Previous studies have reported similar peak asymmetry for different material systems including Inconel 718, Ti-6Al-4V, and high entropy alloys^{15,25,32}. However, the peak shoulders persist even after significant cooling of the sample (top inset in Fig. 3 from 6.8 s to 7.7 s), which we propose is due to the local elemental segregation of Nb and Mo at the interdendritic regions, as expected from AM of IN625^{33,34} (Supplementary Fig. 4a). This is also reported in the literature, where a significant broadening of the 1D peak shapes due to chemical segregation and interdendritic growth associated with peak shoulders is observed^{15,35}. During solidification, the formation of high-temperature peaks of the secondary phase Nb₂C is indicated by orange arrows. Additionally, the presence of another minority secondary phase (S.P.) during the solid state cooling is identified by the red arrow. The compositions of these phases are analyzed using EDS, as shown in Supplementary Fig. 4b, c.

Insights from the operando x-ray diffraction data help us observe and rationalize the different stages of solidification during AM of IN625 according to Fig. 4: During Stage 1, the non-equilibrium nature of the AM process leads to bulk nucleation events in the small melt pools^{36,37}, which last for a very short time and usually grow into crystallites. During Stage 2, two probable events might occur either independently or simultaneously: (i) formation of crystallites and equiaxed dendrites from the bulk nuclei in the melt pool, (ii) dendritic growth due to secondary nucleation from the periphery of the melt pool, starting from the unmelted powders. The growing dendrites would be subject to torsion and bending forces, induced by an interplay of fluid, drag, and gravity forces. During Stage 3, growth of the dendritic and interdendritic channels continues¹⁵, accompanied by microsegregation of Nb in IN625^{38,39}. Some other unique features of this stage include dendrite fragmentation or assimilation phenomena.

Conclusion

This article explores different modes of thermomechanical deformation during AM solidification of Inconel 625. The role of local

thermomechanical deformation during solidification has previously not been studied in the realm of AM; however, our diffraction results show clear differences in thermal versus thermomechanical aspects of the process. The study of both 1D and 2D diffraction data provides a complementary understanding of the solidification mechanisms. From the 1D diffraction data, the analysis of peak shapes, and the formation of interdendritic growth and secondary phases can be performed. However, peak shapes contain a lot of information that will be difficult to deconvolute. In standard 1D diffraction images, the effects of intragranular misorientations are not typically measured as they result in peak spreading perpendicular to the q-vector range²⁵. In those cases, focusing on the 2D analysis can help us understand some of the phenomena in a deconvoluted fashion, as demonstrated in this study. Specifically, the paper describes how different dendritic deformation modes are directly correlated with operando x-ray diffraction signatures: (1) for the deformations caused by torsion and bending, we see a continuous curved line in the azimuth versus time plots for specific lattice planes, (2) for fragmentation/assimilation, we see a single curved line abruptly split into multiple lines; and (3) for the oscillations in the solid cooling, we see the diffraction spots appear and disappear at periodic intervals. Such signatures were verified with the post-mortem EBSD data that were correlated to the 2D diffraction data, providing evidence of the origins of sub-features in the microstructures. Leveraging control of these deformation modes could allow for the introduction of specific microstructural features, such as misorientations, GNDs, and LAGBs, in AM parts. This would provide site-specific design freedom and allow for the tuning of overall mechanical performance of the final as-built parts.

Methods

Operando synchrotron diffraction. The experiments were carried out using a custom-made AM setup designed and built for specialized high-energy x-ray diffraction experiments^{24,40}. The diameter of the focused laser beam spot was 500 μm . Supplementary Fig. 1a shows the setup schematic with an x-ray beam passing through the material and diffracting on the other end, finally reaching the detector. The monochromatic hard x-ray beam energy of 61.3 keV and wavelength 0.202 \AA is irradiated in transmission mode, with a beam size of $250 \times 250 \mu\text{m}^2$. The experiments were powder bed-based line scans. The powder bed dimension was 14 mm \times 2 mm \times 2 mm (L, W, H). The thickness of the printed samples was measured and is close to 1 mm along the x-ray transmission direction. Note that the x-ray beam is fixed at 500 μm from the top surface of the substrate. The x-ray spot constantly probed the center of a 14 mm track. Therefore, we could capture the evolution of the same volume with time, including powder heating, melt pool, transient zone, and solid cooling zones, respectively. This creates a diffraction cone, a part of which is captured by the Mixed Mode Pixel Array Detector (MM-PAD)⁴¹ with a frame rate of 100 Hz. The high energy flux at the FAST beamline is ideal for experiments with thick metallic samples and relatively high atomic number materials like IN625. IN625 (Steward Advanced Materials), with a size range of 45–150 μm , was used for the experiments. IN625 is a solid-solution nickel-based superalloy, majorly strengthened by Nb and Mo in a base Ni-Cr-rich matrix. The experimental processing conditions used were 250 W, 4.5 mm/s.

Data analysis, consideration and interpretations

Data analysis routines. The angular position of a specific diffraction spot was directly derived from the raw 2D images at the maximum intensity. The 2D azimuthal diffraction patterns were plotted using an azimuthal bin size of 10°, and minimum spacing of 0.220°. For every plot of azimuthal angle vs. time, a 2θ range of values for

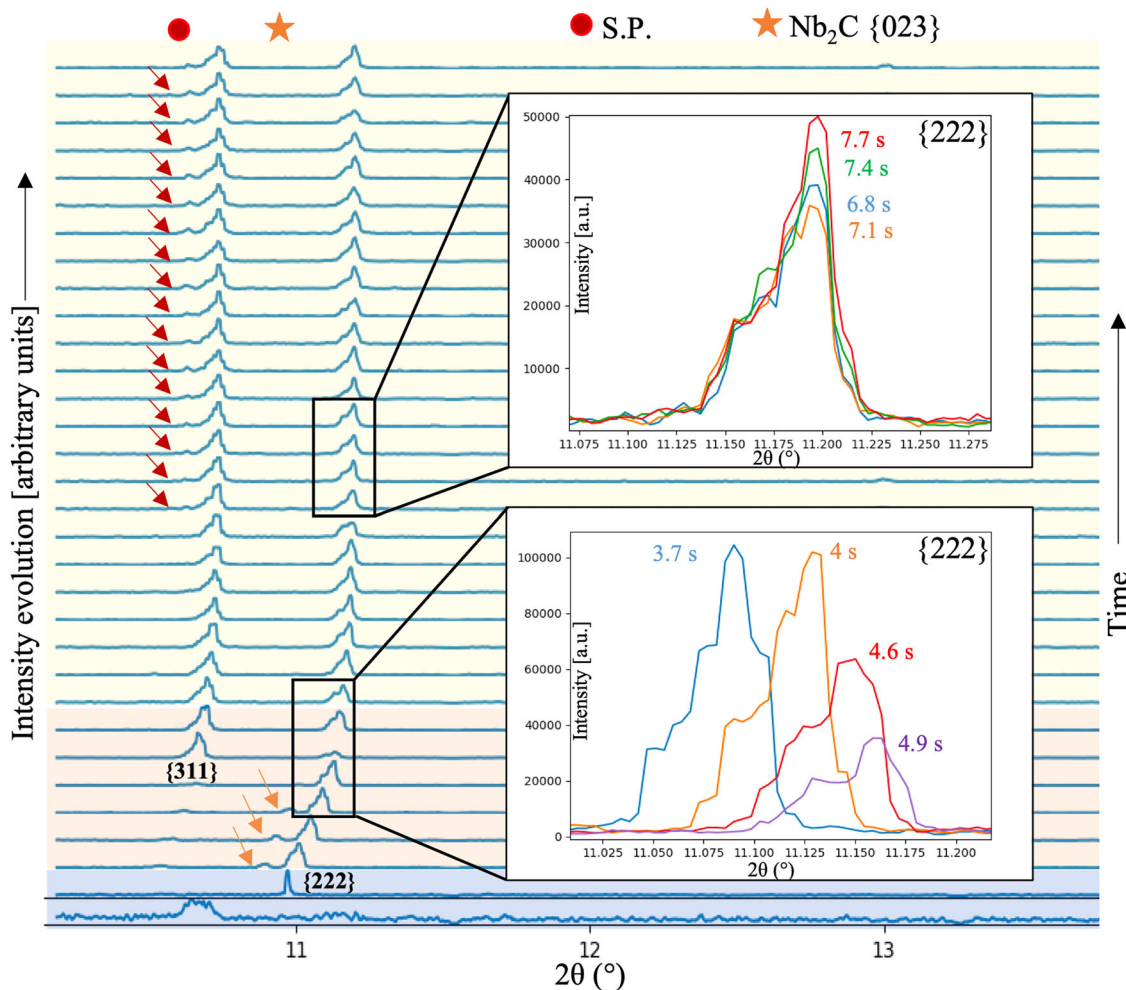


Fig. 3 Stacked plots of integrated 1D x-ray diffraction patterns with time, with orange arrows highlighting the Nb₂C {023} peak. The red arrows indicate the possible appearance of a secondary phase (S.P.) peak during cooling due to microsegregation. Inset: the different cooling regions and associated changes in the 1D {222} peak.

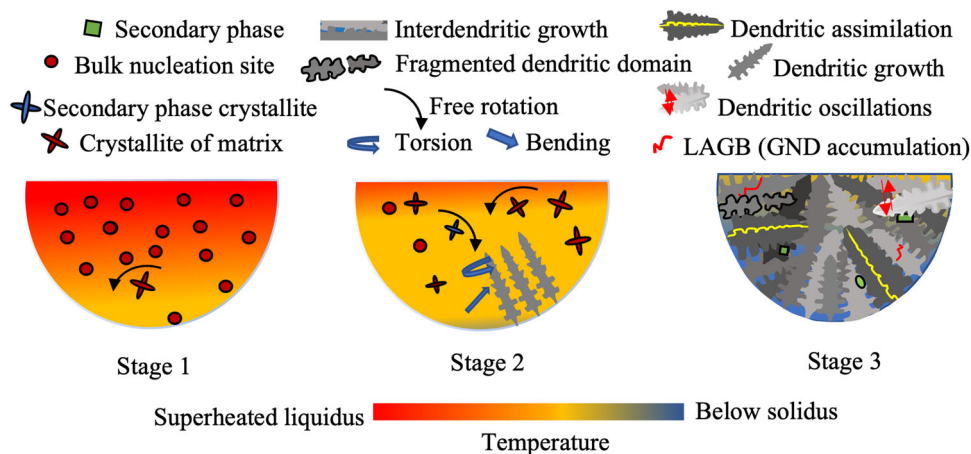


Fig. 4 Schematic showing the three major stages of solidification during AM of IN625. The different gray shades highlight the different dendritic orientations.

different peaks were considered to ensure that the peak shifts during heating and cooling were included correctly in the plot. For every azimuthal bin spacing, the intensity is summed up and repeated across all bins. The 1D diffraction patterns were azimuthally integrated across an azimuthal bin size of 10° with a 2θ unit size of 0.50°.

Based on our setup design, we are probing conditions close to Directed Energy Deposition (DED). In addition, our setup design limits the maximum achievable laser scan speed due to the simultaneous mechanism of stage movement (instead of the laser) and corresponding motion cancellation by the Huber stage at the

beamline²⁴. The choice of scan speed (4.5 mm/s) was limited by factors such as minimum exposure time of x-rays such that the detector captures a good signal-to-noise ratio. The MMPAD detector position provided a q-coverage ranging from 5.51 to 8.07 Å⁻¹ ($Q = 4\pi \sin\theta/\lambda$) when located 640 mm away from the sample at the x-ray energy of 61.3 keV. The detector consists of a 2 × 3 tiled

$$g\{\phi_1, \phi, \phi_2\} = \begin{matrix} \cos \phi_1 \cos \phi_2 - \sin \phi_1 \sin \phi_2 \cos \phi & \sin \phi_1 \cos \phi_2 + \cos \phi_1 \sin \phi_2 \cos \phi & \sin \phi_2 \sin \phi \\ -\cos \phi_1 \sin \phi_2 - \sin \phi_1 \cos \phi_2 \cos \phi & -\sin \phi_1 \sin \phi_2 + \cos \phi_1 \cos \phi_2 \cos \phi & \cos \phi_2 \sin \phi \\ \sin \phi_1 \sin \phi & -\cos \phi_1 \sin \phi & \cos \phi \end{matrix} \quad (1)$$

array that comprises 256 pixels × 384 active pixels and is linked to a 0.75 mm thick CdTe sensor. With a pixel size of 150 μm × 150 μm and full well depths of 4.6 × 10⁸ keV, these detector attributes allow for x-ray imaging at energies beyond 100 keV and a maximum achievable frame rate of 1 kHz⁴². To achieve a good signal-to-noise ratio on the detector, a frame rate of 100 Hz (10 ms exposure) was used for the experiments in this study. The data was calibrated in-house at CHESS using a custom code for the MMPAD. For this purpose, the Ceria calibrant was used as a reference standard, and images were collected at 0° and 180°. The code optimizes for detector positions (including tilt) and sample-to-detector distance (~640 mm). We used a package written in-house to analyze the operando diffraction data. The detector distance calibration, background subtraction, azimuthal integration, and averaging are performed using HEXRD and MMPADUTIL open-source Python-based scripts developed at the CHESS. Most data analysis routines and plots are generated using Python, matplotlib, Scipy, and NumPy packages.

Scanning electron microscopy: EDS & EBSD analysis. The samples were cross-sectioned along the center and the build direction. The sample preparation included surface finish down to 0.02 μm using standard metallographic procedures. This helped achieve a good surface finish to successfully perform EBSD on the Tescan MIRA3 field emission scanning electron microscope (FE-SEM). The window size of the EBSD image covers a 200 μm × 240 μm cross-sectional area. High-resolution EDS was also performed on an area of interest to study elemental segregation. Point-based EDS analysis was performed to identify the secondary phases. For EDS analyses, the atomic weight % of elements was considered. EBSD and EDS data were collected using the QUANTAX EBSD (Bruker, Billerica, MA, USA) application. ATEX and MTEX softwares were used for detailed analyses of the EBSD dataset.

Correlation between EBSD and synchrotron x-ray diffraction. Supplementary 7a explains the coordinate system of the EBSD detector and the hutch coordinate system comprising X, Y, and Z axes demonstrating the x-ray beam direction, the laser beam direction, and the laser scan direction, respectively. Supplementary Fig. 7b illustrates the rotated orientation matrix as calculated based on the Euler angle of the grain of interest with respect to the hutch coordinate system. It also shows the position of the new vector of interest for the given {222} plane. Supplementary Fig. 7c demonstrates the angle between the constructed and XY planes for one such grain. The detector sits on the YZ plane; therefore, the calculated angle would be the shift along the azimuth from its mean position (90°).

The following steps are followed in this study to identify grains diffracting along our recorded x-ray azimuth range:

1. The convention used in this EBSD image is ‘Bunge’ Euler; hence a sequence of ‘ZXZ’ rotations is performed. ATEX software is used to prepare the Euler Angles Map, using the convention { ϕ_1, ϕ, ϕ_2 }.
2. The corresponding orientation matrix is generated with the following rotation matrix { $R\phi_1, R\phi, R\phi_2$ }⁴³:

3. Expressing the diffraction plane vector of {222} family of planes corresponding to any of its eight combinations from the crystal frame to the hutch coordinate system (same as the EBSD detector coordinate system):

$$V_s = g^{-1} \cdot V_c \quad (2)$$

where V_s is a vector in the sample frame, V_c is a vector in the crystal frame, and g is the new orientation matrix.

4. Once the new 3D vector of the {222} plane set in the new coordinate system is obtained, we can generate a plane equation in which the normal of each of the {222} planes lie. For this, the three points are the origin (0,0,0), the x-ray beam (i.e., the X-axis in the hutch coordinate system), and the new 3D vector. All these points should lie on that plane. However, due to the multiplicity of the {222} family of planes, eight possible combinations of this plane should be considered when trying to map the different spots in the x-ray detector with the post-processed EBSD image.
5. The final step is finding the angle between the mean position of the detector (it was sitting at the top center) and the plane equation generated in point 4. XY plane is the plane that cuts through vertically and perpendicular to the detector. We use the generated plane equation and $z = 0$ (XY plane in the hutch coordinate system) to find this angle. The assumption is that the detector has no tilt and sits fully flat on the ZY plane. The following equation could be used to calculate this angle:

$$\alpha = \cos^{-1} \frac{|A1.A2 + B1.B2 + C1.C2|}{\sqrt{A1^2 + B1^2 + C1^2} \cdot \sqrt{A2^2 + B2^2 + C2^2}} \quad (3)$$

where $A1, B1, C1$, and $A2, B2, C2$ are the coefficients of the two planes, i.e., the XY plane and the plane equation developed in (4) according to the specific {222} hkl plane.

Code availability

The codes associated with this work are available upon reasonable request to the corresponding author.

Data availability

The data associated with this work are available upon reasonable request to the corresponding author.

Received: 28 December 2022; Accepted: 16 September 2023;

Published online: 10 October 2023

References

1. DebRoy, T. et al. Additive manufacturing of metallic components – process, structure and properties. *Prog. Mater. Sci.* **92**, 112–224 (2018).

2. Sames, W. J., List, F. A., Pannala, S., Dehoff, R. R. & Babu, S. S. *The Metallurgy and Processing Science of Metal AM.pdf*. <https://www.osti.gov/servlets/purl/1267051> (2016).
3. Grosse, S., Hutchinson, C., Gouné, M. & Banerjee, R. Additive manufacturing of metals: a brief review of the characteristic microstructures and properties of steels, Ti-6Al-4V and high-entropy alloys. *Sci. Technol. Adv. Mater.* **18**, 584–610 (2017).
4. Lewandowski, J. J. & Seifi, M. Metal additive manufacturing: a review of mechanical properties. *Annu. Rev. Mater. Res.* **46**, 151–186 (2016).
5. Dass, A. & Moridi, A. State of the art in directed energy deposition: from additive manufacturing to materials design. *Coatings* **9**, 418 (2019).
6. Alipour, S., Moridi, A., Liou, F. & Emdadi, A. The trajectory of additively manufactured titanium alloys with superior mechanical properties and engineered microstructures. *Addit. Manuf.* **60**, 103245 (2022).
7. Zhang, D. et al. Metal alloys for fusion-based additive manufacturing. *Adv. Eng. Mater.* **20**, 1700952 (2018).
8. Carroll, B. E., Palmer, T. A. & Beese, A. M. Anisotropic tensile behavior of Ti-6Al-4V components fabricated with directed energy deposition additive manufacturing. *Acta Mater* **87**, 309–320 (2015).
9. Wakai, A., Das, A., Bustillos, J. & Moridi, A. Effect of solidification pathway during additive manufacturing on grain boundary fractality. *Addit. Manuf. Lett.* **6**, 100149 (2023).
10. Todaro, C. J. et al. Grain structure control during metal 3D printing by high-intensity ultrasound. *Nat. Commun.* **11**, 142 (2020).
11. Zhang, D. et al. Additive manufacturing of ultrafine-grained high-strength titanium alloys. *Nature* **576**, 91–95 (2019).
12. Tiller, W. A., Jackson, K. A., Rutter, J. W. & Chalmers, B. The redistribution of solute atoms during the solidification of metals. *Acta Metall* **1**, 428–437 (1953).
13. Strickland, J., Nenchev, B. & Dong, H. On directional dendritic growth and primary spacing—a review. *Crystals* **10**, 627 (2020).
14. Ruan, Y., Mohajerani, A. & Dao, M. Microstructural and mechanical-property manipulation through rapid dendrite growth and undercooling in an Fe-based Multinary Alloy. *Sci. Rep.* **6**, 31684 (2016).
15. Schneiderman, B., Chuang, A. C., Kenesei, P. & Yu, Z. In situ synchrotron diffraction and modeling of non-equilibrium solidification of a MnFeCoNiCu alloy. *Sci. Rep.* **11**, 1–12 (2021).
16. Clarke, A. J. et al. X-ray imaging and controlled solidification of Al-Cu alloys toward microstructures by design. *Adv. Eng. Mater.* **17**, 454–459 (2015).
17. Aveson, J. W. et al. Dendrite bending during directional solidification. *Superalloys 2012* 615–624 <https://doi.org/10.1002/9781118516430.ch69> (2012).
18. Aveson, J. W. et al. On the deformation of dendrites during directional solidification of a Nickel-based superalloy. *Metall. Mater. Trans. A Phys. Metall. Mater. Sci.* **50**, 5234–5241 (2019).
19. Mathiesen, R. H., Arnberg, L., Bleuet, P. & Somogyi, A. Crystal fragmentation and columnar-to-equiaxed transitions in Al-Cu studied by Synchrotron x-ray video microscopy. *Metall. Mater. Trans. A Phys. Metall. Mater. Sci.* **37**, 2515–2524 (2006).
20. Yasuda, H. et al. Dendrite fragmentation induced by massive-like δ - γ transformation in Fe-C alloys. *Nat. Commun.* **10**, 1–5 (2019).
21. Mckeown, J. T., Clarke, A. J. & Wizeczek, J. M. K. Imaging transient solidification behavior. *MRS Bull* **45**, 916–926 (2020).
22. Clarke, A. et al. Proton radiography peers into metal solidification. *Sci. Rep.* **3**, 1–6 (2013).
23. Polonsky, A. T. et al. Solidification-driven orientation gradients in additively manufactured stainless steel. *Acta Mater* **183**, 249–260 (2020).
24. Dass, A., Gabourel, A., Pagan, D. C. & Moridi, A. Laser-based directed energy deposition system for operando synchrotron x-ray experiments. *Rev. Sci. Instrum.* **075106**, 075106-1–075106-9 (2022).
25. Pagan, D. C., Jones, K. K., Bernier, J. V. & Phan, T. Q. A finite energy bandwidth-based diffraction simulation framework for thermal processing applications. *Jom* **72**, 4539–4550 (2020).
26. Huang, Z. et al. Grain rotation and lattice deformation during photoinduced chemical reactions revealed by in situ X-ray nanodiffraction. *Nat. Mater.* **14**, 691–695 (2015).
27. Yonemura, M. et al. In-situ observation for weld solidification in stainless steels using time-resolved X-ray diffraction. *Mater. Trans.* **47**, 310–316 (2006).
28. Medvedev, D., Varnik, F. & Steinbach, I. Simulating mobile dendrites in a flow. *Procedia Comput. Sci.* **18**, 2512–2520 (2013).
29. Sun, S., Adams, B. L. & King, W. E. Observations of lattice curvature near the interface of a deformed aluminium bicrystal. *Philos. Mag. A Phys. Condens. Matter, Struct. Defects Mech. Prop.* **80**, 9–25 (2000).
30. Pantleon, W. Resolving the geometrically necessary dislocation content by conventional electron backscattering diffraction. *Scr. Mater.* **58**, 994–997 (2008).
31. Boley, B. A. Thermally induced vibrations of beams. *J. Astronaut. Sci.* **23**, 179–181 (1956).
32. Hocine, S. et al. Operando X-ray diffraction during laser 3D printing. *Mater. Today* **34**, 30–40 (2020).
33. Lass, E. A. et al. Formation of the Ni₃Nb δ -phase in stress-relieved inconel 625 produced via laser powder-bed fusion additive manufacturing. *Metall. Mater. Trans. A Phys. Metall. Mater. Sci.* **48**, 5547–5558 (2017).
34. Keller, T. et al. Application of finite element, phase-field, and CALPHAD-based methods to additive manufacturing of Ni-based superalloys. *Acta Mater* **139**, 244–253 (2017).
35. Čapek, J. et al. The effect of γ'' and δ phase precipitation on the mechanical properties of inconel 718 manufactured by selective laser melting: an in situ neutron diffraction and acoustic emission study. *Jom* **73**, 223–232 (2021).
36. Thampy, V. et al. Subsurface cooling rates and microstructural response during laser based metal additive manufacturing. *Sci. Rep.* **10**, 1–9 (2020).
37. Martin, J. H. et al. 3D printing of high-strength aluminium alloys. *Nature* **549**, 365–369 (2017).
38. Chen, W. Composition effects on macroscopic solidification segregation of superalloys. (West Virginia University, 2000).
39. Young, G. A., Hackett, M. J., Tucker, J. D. & Capobianco, T. E. Welds for Nuclear Systems. *Compr. Nucl. Mater. Second Ed.* 517–544 <https://doi.org/10.1016/B978-0-12-803581-8.11689-3> (2020).
40. Dass, A. Fundamentals of solidification in directed energy deposition type additive manufacturing of inconel 625. *ProQuest Dissertations and Theses* (Cornell University, 2020).
41. Becker, J. et al. High-speed imaging at high x-ray energy: CdTe sensors coupled to charge-integrating pixel array detectors. *AIP Conf. Proc.* **1741**, 1–5 (2016).
42. Philipp, H. T., Tate, M. W., Shanks, K. S., Purohit, P. & Gruner, S. M. High dynamic range CdTe mixed-mode pixel array detector (MM-PAD) for kilohertz imaging of hard x-rays. *J. Instrum.* **15**, P06025-1–P06025-11 (2020).
43. Rowenhorst, D. et al. Consistent representations of and conversions between 3D rotations. *Model. Simul. Mater. Sci. Eng.* **23**, 083501-1–083501-22 (2015).

Acknowledgements

Research supported by the National Science Foundation (NSF) early career award #CMM1-2046523, (operando diffraction studies) by the U.S. department of Energy (DOE), office of science, basic energy science (BES) early career award # DE-SC0022860 (data analysis tools). This work made use of the Cornell Center of Materials Research Shared Facilities, which are supported through the NSF MRSEC program [DMR-1719875]. This work is based upon research conducted at the Center for High Energy X-ray Sciences (CHEXS), which is supported by the National Science Foundation [DMR-1829070]. The authors would like to acknowledge Shonak Bhattacharya and the Cornell High Energy Synchrotron Source staff for help during the beamtime. We also acknowledge Dr. Hugh Philipp, and Dr. Mark W. Tate for help with setting up the MM-PAD detector for the operando experiments. A.M. also acknowledges Prof. Anthony Rollett for fruitful discussions.

Author contributions

A.D. contributed to the conceptualization, investigation, writing, review & editing, methodology, and data curation. D.C.P. contributed to the methodology, investigation and review & editing of the scientific work. A.M. contributed to the conceptualization, investigation, review & editing of the scientific work and funding acquisition. A.D., C.T., D.C.P. and A.M. performed experiments at the synchrotron.

Competing interests

The authors declare no competing interests.

Additional information

Supplementary information The online version contains supplementary material available at <https://doi.org/10.1038/s43246-023-00404-0>.

Correspondence and requests for materials should be addressed to Atieh Moridi.

Peer review information *Communications Materials* thanks Wentao Yan and the other, anonymous, reviewer(s) for their contribution to the peer review of this work. Primary Handling Editors: Cang Zhao and John Plummer.

Reprints and permission information is available at <http://www.nature.com/reprints>

Publisher's note Springer Nature remains neutral with regard to jurisdictional claims in published maps and institutional affiliations.



Open Access This article is licensed under a Creative Commons Attribution 4.0 International License, which permits use, sharing, adaptation, distribution and reproduction in any medium or format, as long as you give appropriate credit to the original author(s) and the source, provide a link to the Creative Commons license, and indicate if changes were made. The images or other third party material in this article are included in the article's Creative Commons license, unless indicated otherwise in a credit line to the material. If material is not included in the article's Creative Commons license and your intended use is not permitted by statutory regulation or exceeds the permitted use, you will need to obtain permission directly from the copyright holder. To view a copy of this license, visit <http://creativecommons.org/licenses/by/4.0/>.

© The Author(s) 2023